Imaging scatterometry of butterfly wing scales

Stavenga, D. G.; Leertouwer, H. L.; Pirih, P.; Wehling, M. F.

Published in:
Optics Express

Publication date:
2009

Link to publication in University of Groningen/UMCG research database

Imaging scatterometry of butterfly wing scales

D.G. Stavenga,[1*] H.L. Leertouwer,[1] P. Pirih,[1] and M.F. Wehling[2]

[1]Department of Neurobiophysics, University of Groningen,
Nijenborgh 4, NL-9747 AG Groningen, The Netherlands
[2]Air Force Research Laboratory, Eglin Air Force Base, FL 32542-6810, USA
[*]Corresponding author: *D.G.Stavenga@rug.nl*

Abstract: We describe an imaging scatterometer allowing hemispherical reflectance measurements as a function of the angle of incidence. The heart of the scatterometer is an ellipsoidal reflector, which compresses the hemispherical reflection into a cone-shaped beam that can be imaged by a normal optical system. The instrument's performance is illustrated by measurements of the scattering profiles of the blue-iridescent dorsal wing scales of the nymphalid *Morpho aega* and the matte-green ventral wing scales of the lycaenid *Callophrys rubi*.

© 2008 Optical Society of America

OCIS codes: (120.1840) Reflectometers; (290.1483) BRDF; (290.5820) Scattering measurements.

References and links

1. M. Srinivasarao, "Nano-optics in the biological world: Beetles, butterflies, birds and moths," Chem. Rev. **99**, 1935-1961 (1999).
2. P. Vukusic and J. R. Sambles, "Photonic structures in biology," Nature **424**, 852-855 (2003).
3. S. Kinoshita and S. Yoshioka, "Structural colors in nature: the role of regularity and irregularity in the structure," ChemPhysChem **6**, 1-19 (2005).
4. K. Kertész, Z. Bálint, Z. Vertésy, G. I. Márk, V. Lousse, J. P. Vigneron, M. Rassart, and L. P. Biró, "Gleaming and dull surface textures from photonic-crystal-type nanostructures in the butterfly *Cyanophrys remus*," Phys. Rev. E **74**, 021922 (2006).
5. K. Michielsen and D. G. Stavenga, "Gyroid cuticular structures in butterfly wing scales: biological photonic crystals," J. R. Soc. Interface **5**, 85-94 (2008).
6. H. Ghiradella and W. Radigan, "Development of butterfly scales: II. Struts, lattices and surface tension," J. Morphol. **150**, 279-297 (1976).
7. H. F. Nijhout, *The Development and Evolution of Butterfly Wing Patterns* (Washington, Smithsonian Institution Press, 1991).
8. H. Ghiradella, "Structure of iridescent lepidopteran scales: variations on several themes," Ann. Entomol. Soc. Am. **77**, 637-645 (1984).
9. D. G. Stavenga, M. A. Giraldo, and B. J. Hoenders, "Reflectance and transmittance of light scattering scales stacked on the wings of pierid butterflies," Opt. Express **14**, 4880-4890 (2006).
10. M. A. Giraldo and D. G. Stavenga, "Sexual dichroism and pigment localization in the wing scales of *Pieris rapae* butterflies," Proc. R. Soc. B **274**, 97-102 (2007).
11. N. I. Morehouse, P. Vukusic, and R. Rutowski, "Pterin pigment granules are responsible for both broadband light scattering and wavelength selective absorption in the wing scales of pierid butterflies," Proc. R. Soc. B **274**, 359-366 (2007).
12. D. G. Stavenga, S. Stowe, K. Siebke, J. Zeil, and K. Arikawa, "Butterfly wing colours: scale beads make white pierid wings brighter," Proc. R . Soc. Lond. B **271**, 1577-1584 (2004).
13. C. W. Mason, "Structural colors in insects. 2.," J. Phys. Chem. **31**, 321-354 (1927).
14. P. Vukusic, J. R. Sambles, C. R. Lawrence, and R. J. Wootton, "Quantified interference and diffraction in single *Morpho* butterfly scales," Proc. R. Soc. Lond. B **266**, 1403-1411 (1999).
15. S. Kinoshita, S. Yoshioka, and K. Kawagoe, "Mechanisms of structural colour in the *Morpho* butterfly: cooperation of regularity and irregularity in an iridescent scale," Proc. R. Soc. Lond. B **269**, 1417-1421 (2002).
16. S. Yoshioka and S. Kinoshita, "Structural or pigmentary? Origin of the distinctive white stripe on the blue wing of a *Morpho* butterfly," Proc. R. Soc. B **273**, 129-134 (2006).
17. M. A. Giraldo, S. Yoshioka, and D. G. Stavenga, "Far field scattering pattern of differently structured butterfly scales," J. Comp. Physiol. A **194**, 201-207 (2008).

18. F. E. Nicodemus, J. C. Richmond, J. J. Hsia, I. W. Ginsberg, and T. Limperis, *Geometrical Considerations and Nomenclature for Reflectance* (Washington, DC, National Bureau of Standards, US Department of Commerce, 1977).
19. R. B. Morris, "Iridescence from diffraction structures in the wing scales of *Callophrys rubi*, the Green Hairstreak," J. Ent. (A) **49**, 149-154 (1975).
20. Y. L. Pan, K. B. Aptowicz, R. K. Chang, M. Hart, and J. D. Eversole, "Characterizing and monitoring respiratory aerosols by light scattering," Opt. Lett. **28**, 589-591 (2003).
21. K. B. Aptowicz, Y. L. Pan, R. K. Chang, R. G. Pinnick, S. C. Hill, R. L. Tober, A. Goyal, T. Leys, and B. V. Bronk, "Two-dimensional angular optical scattering patterns of microdroplets in the mid infrared with strong and weak absorption," Opt. Lett. **29**, 1965-1967 (2004).
22. O. G. Rodríguez-Herrera, M. Rosete-Aguilar, and N. C. Bruce, "Scatterometer of visible light for 2D rough surfaces," Rev. Sci. Instr. **75**, 4820-4823 (2004).
23. S. Yoshioka and S. Kinoshita, "Wavelength-selective and anisotropic light-diffusing scale on the wing of the *Morpho* butterfly," Proc. R. Soc. B **271**, 581-587 (2004).
24. S. Berthier, *Iridescences, les Couleurs Physiques des Insectes* (Paris, Springer, 2003).
25. P. Vukusic and D. G. Stavenga, "Physical methods for investigating structural colours in biological systems," J. R. Soc. Interface, in press (2009).
26. B. D. Wilts, H. L. Leertouwer, and D. G. Stavenga, "Imaging scatterometry and microspectrophotometry of lycaenid butterfly wing scales with perforated multilayers," J. R. Soc. Interface, in press (2009).

1. Introduction

The interaction of light with material bodies is generally studied by measuring the reflection and transmission, or more generally their scattering properties. A research area with many unsolved light scattering questions, which has recently witnessed an explosive increase in attention, is that of the photonic crystals. Special attention in that area is taken up by the wing scales of butterflies [1-5]. However, the scale structures are often intricate, and the resulting optical properties accordingly are difficult to analyze.

Butterfly wing scales resemble flattened sacs, a few micrometers thick, and with length and width in the order of 200 and 75 μm, respectively [6,7]. The lower lamina of a butterfly wing scale is virtually always more or less smooth, but the upper lamina is commonly highly structured. It consists of parallel, longitudinal ridges, spaced apart by 1 to 2 μm, which are connected by crossribs, with separation 0.5 to 1 μm [6]. The space between upper and lower lamina can be almost empty or it can be highly structured, depending on the butterfly species and the scale type [8]. The scale material can be virtually transparent or it can contain strongly absorbing pigment. The structuring of the scale together with the physical properties of its material components determine how incident light is absorbed and scattered by the scale, and thus the scales determine the coloration of their owners [7,9]. For instance, the scales of pierid butterflies are packed with beads, 100-200 nm sized granules attached to the crossribs, which contain light-absorbing pigments [10,11]. Although the wings of pierids thus are said to have pigmentary colors, the observed light reflections are, of course, due to scattering by the strongly irregularly organized wing scales [12].

In many butterflies, the scales feature regular structures, resulting in so-called structural colors. The best studied example is the *Morpho* scale type, where the ridges form multilayers that act as highly effective blue reflectors [13]. Vukusic et al. [14] studied *Morpho* scales by focusing monochromatic laser beams at a single, isolated scale. They measured the scattering profile by scanning a detector around the scale. Kinoshita et al. [15], in a similar approach, applied a broad-band, white light beam, and measured the angular-dependent reflectance with a scanning fiber optic. Additionally, they visualized the scattering pattern on a screen, which had a small hole through which the illuminating light beam passed before hitting the scale. It thus appeared that a normally irradiated *Morpho* scale creates an approximately line-shaped far-field scattering profile, in the plane perpendicular to the ridges, due to diffraction by the narrow ridges [15-17].

Measuring the scattered beam with a narrow-aperture, scanning detector is very laborious, and quantification of photographs of the scattered light distribution on a screen is a quite insensitive procedure. We therefore have developed as an alternative an imaging

scatterometer, which projects the full hemispherical scattering on a digital camera. Here we describe the scatterometer and illustrate its workings on scales of two structurally colored butterflies, the nymphalid *Morpho aega* and the lycaenid *Callophrys rubi*.

2. Materials and methods

2.1. Butterfly scales

A small piece, about 2 mm x 2 mm, cut from the wings of a butterfly, was glued to the tip of a glass micropipette. Subsequently, the micropipette was mounted on a micromanipulator, which allowed precise adjustment of a scale in the first focal point of the ellipsoidal reflector of the scatterometer (Fig. 1).
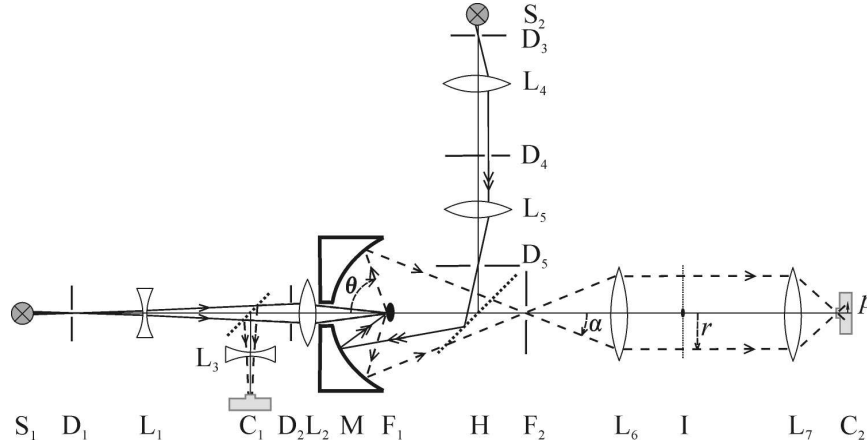

Fig. 1. Diagram of the imaging scatterometer. The primary beam, delivered by light source S_1 and diaphragm D_1, is focused by lenses L_1 and L_2, via a central hole in the ellipsoidal reflector, M, on the sample, positioned in the first focal point of the reflector, F_1. The positioning of the sample is visually controlled with the epi-illumination microscope consisting of lenses L_2 and L_3 to which camera C_1 is connected. The beam aperture is determined by diaphragm D_2. The secondary beam, delivered by light source S_2, via diaphragms D_{3-5} and lenses L_4 and L_5, is focused via a beam splitter, H, and the ellipsoidal reflector at the sample. Light scattered by the sample is focused at the second focal point of the reflector, F_2, which coincides with the front-focal point of a large-aperture photographical lens, L_6. The far-field scattering pattern, projected in plane I, is imaged by lens L_7 at a digital camera, C_2. A reflected light ray, having an angle θ with the axis, leaves the second focal point with an angle α, has a distance r to the axis in the back focal plane of lens L_6, and is projected at the camera chip at a distance p from the axis. A spatial filter in plane I blocks the zeroth-order transmitted light.

2.2. Imaging scatterometry

The imaging scatterometer, diagrammatically shown in Fig. 1, was inspired by the setup of Kinoshita et al. [15], where a small diaphragm, illuminated by a xenon lamp, is projected at a butterfly scale via a small hole in a white screen, and the light scattered by the scale is secondarily scattered by the screen. We have replaced the white screen by an ellipsoidal reflector, which has a small, central hole. The study object, for instance a butterfly scale, isolated or attached to a wing fragment, is positioned in the first focal point, F_1, of the reflector, M (Fig. 1). The primary beam is supplied by light source S_1. It illuminates field diaphragm D_1, which is focused by lenses L_1 and L_2 at the sample in F_1. The aperture diaphragm D_2 limits the beam to within the hole in the ellipsoid. The approximately axially back-scattered (reflected) light that returns throughout the hole in the reflector is then, via a half-mirror, focused by lenses L_2 and L_3 at camera C_1, which is connected to a binocular viewer.

The secondary beam illuminates diaphragm D_3, which is focused by lenses L_4 and L_5 on diaphragm D_5. The aperture diaphragm D_4 and the field diaphragm D_5 are positioned in the front and back focal planes of lens L_5, respectively. The planes of D_5 and F_2 are conjugated via beam splitter H. The secondary beam reaches the sample via beam splitter H and the ellipsoidal reflector. The angle of incidence of the secondary light beam at the sample is varied by laterally moving D_4.

Light that is back-scattered by the sample in off-axis directions is reflected by the ellipsoid and then proceeds through a diaphragm in the plane of the second focal point F_2. The sample's far-field scattering pattern thus is imaged in the back-focal plane I of lens L_6, and subsequently lens L_7 focuses that plane at camera C_2. A spatial filter in plane I, together with the diaphragm in the plane of F_2, suppresses the light transmitted by the sample.

The micromanipulator carrying the micropipette with the butterfly wing piece (or with a single scale) allows rotation around its axis. Using the primary beam, this allows measurement of the scattering pattern as a function of the angle of incidence, however only for light incident in a plane perpendicular to the rotation axis. The dependence of the scattering pattern from any angle of incidence can be measured by using the secondary light beam and moving diaphragm D_4 laterally, that is vertically and/or horizontally.

We note here that the transmittance characteristics of a scale can be studied by centering D_4, on the axial position, so that the sample is axially illuminated, from the reverse side. The transmitted light is then reflected by the ellipsoidal mirror and, after focusing at F_2, is then again imaged at camera C_2.

The components of the imaging scatterometer as realized in our laboratory are as follows. Light sources $S_{1,2}$: xenon lamps; lenses $L_{1,3,4}$: Spindler & Hoyer lenses with focal distances -40, -100, 90 mm, respectively; L_2: Zeiss Luminar 16 mm; L_5: Mamiya-Sekor 55/1.8; L_6: AF Nikor 50/1.8; L_7: Wollensak 75/1.9. The beam splitter H is a pellicle. The ellipsoidal reflector, M, symmetric around the major axis, is an aluminum mirror (produced on order by TNO I&T, Delft, the Netherlands). The semi-major and semi-minor axes are $a = 100$ mm and $b = 57.2$ mm, respectively, so that, with $c = \sqrt{(a^2-b^2)}$, the distance between the focal points $F_1F_2 = 2c = 164$ mm, and the eccentricity of the reflector $\varepsilon = c/a = 0.82$. The diameter of the reflector is 65.5 mm, so that the focal point is in the plane of the rim of the reflector. In other words, the rim corresponds to $\theta = 90^\circ$, that is, the reflector captures exactly a hemispherical spatial angle. The diameter of the central hole in the mirror is 3.2 mm, so that an angular aperture of 10.2° is lost from the scattering pattern. For collecting the images (by camera C_2) we use an Olympus DP70 digital camera (4080x3072 pixels; for RGB color images), or a Photometrics Coolsnap ES monochrome digital camera (1392x1040 pixels). For observing the sample with camera C_1, we use a Jenoptik ProgRes C10 or the Olympus DP70.

2.3. Imaging with an ellipsoidal mirror

Consider the ellipsoidal mirror, symmetric around the major axis, where a light ray leaves the first focal point, F_1, with an angle θ with respect to the major axis (Fig. 1). After reflection it passes the second focal point, F_2, with an angle α given by:

$$\alpha = \text{asin}[(1-\varepsilon^2)\sin\theta/(1+\varepsilon^2+2\varepsilon\cos\theta)] \qquad (1a)$$

where ε is the eccentricity of the ellipsoid. For the extreme angle $\theta_{max} = 90^\circ$,

$$\alpha_{max} = \text{asin}[(1-\varepsilon^2)/(1+\varepsilon^2)] \qquad (1b)$$

With $\varepsilon = 0.82$ it follows that $\alpha_{max} = 11.3^\circ$, which is well within the 15.5° aperture of lens L_6.

If f_6 is the focal length of lens L_6, then the distance of the light ray in the back-focal plane I of lens L_6 equals $r = \alpha f_6$ (with $\alpha = \tan\alpha$ in radian, as $\alpha < \alpha_{max} = 0.197$ is sufficiently small). The light ray with angle θ hence arrives at a distance $p = mr = m\alpha f_6 = M\alpha$ from the axis, with m the magnification of the imaging by lens L_7, and $M = mf_6$. For a reflected beam with an extreme angle of $\theta_{max} = 90^\circ$, the pixel distance is $p_{max} = M\alpha_{max}$, so that the relative pixel distance is:

$$p^* = p/p_{max} = \alpha/\alpha_{max} \tag{1c}$$

2.4. Corrections of the scatterometer images

The scatterometer allows direct visualization of the Bidirectional Reflectance Distribution Function (BRDF; dimension: sr^{-1}) for an incident light beam from any chosen direction (θ_i, φ_i); see Fig. 2(a). The BRDF is defined as the ratio between the reflected radiance $L_r(\theta_r, \varphi_r)$ (dimension: $W\ m^{-2}\ sr^{-1}$) and the incident irradiance $E_i(\theta_i, \varphi_i)$ (dimension: $W\ m^{-2}$) [18]:

$$R_\lambda(\theta_i, \varphi_i, \theta_r, \varphi_r) = \frac{L_r(\theta_r, \varphi_r) d\omega_r}{E_i(\theta_i, \varphi_i)\cos\theta_i\, d\omega_i} \tag{2}$$
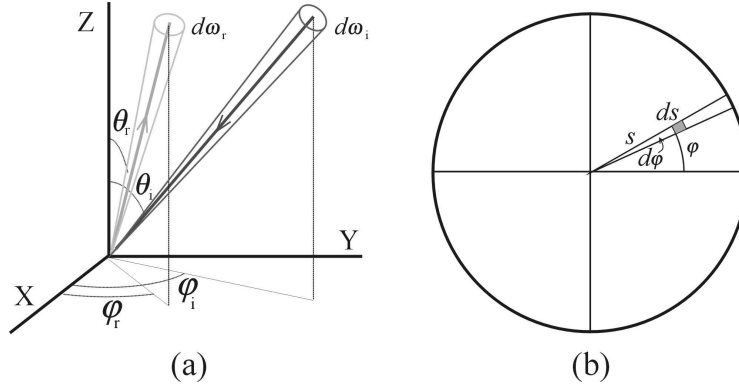
Fig. 2. Coordinate systems for the spatial relationships of light fluxes. (a) The bidirectional reflectance distribution function relates the reflected radiance $L_r(\theta_r, \varphi_r)$ with the incident irradiance $E_i(\theta_i, \varphi_i)$; see Eq. 2. (b) Polar diagram where the area of the spatial element (grey) equals $d\sigma = s\, ds\, d\varphi$. The coordinate s is the pixel distance p or the angle θ_r, and $\varphi = \varphi_r$.

Light reflected into direction (θ_r, φ_r) is projected at position (p, φ_r) of camera C_2 (Fig. 1), where p is the distance from the axial pixel (see Fig. 2(b)). The radial coordinate p is proportional to the angle α: $p = M\alpha$ (section 2.3), but α is non-linearly related to the angle $\theta = \theta_r$ (Eq. 1a), and therefore the spatial light distribution captured by the camera is not a perfect polar diagram for (θ_r, φ_r). For obtaining such a diagram the images have to be corrected as follows.

In the spherical coordinate system with origin F_1 the radiant intensity $I_r(\theta_r, \varphi_r)$ (dimension: $W\ sr^{-1}$) is scattered into the direction (θ_r, φ_r). $I_r(\theta_r, \varphi_r) d\omega_r$, the light power scattered by the sample into the spatial angle $d\omega_r = \sin\theta_r\, d\theta_r\, d\varphi_r$, is projected at an area $d\sigma = p\, dp\, d\varphi_r$ of the camera chip (Fig. 2(b), with $s = p$), and thus it equals the light power $E_{cam}(p, \varphi_r) d\sigma$, where $E_{cam}(p, \varphi_r)$ is the irradiance received by the camera. In order to obtain the irradiance in the polar coordinate system with coordinates (θ_r, φ_r), E_{cam} has to be corrected with the condition $E_{cor}\theta_r\, d\theta_r\, d\varphi_r = E_{cam}\, p\, dp\, d\varphi_r$, where $E_{cor}(\theta_r, \varphi_r)$ is the corrected irradiance. Dropping the suffix r, we obtain (with $p = M\alpha$):

$$E_{cor} = E_{cam}\frac{p}{\theta}\frac{dp}{d\theta} = E_{cam}M^2\frac{\alpha}{\theta}\frac{d\alpha}{d\theta} = E_{cam}K \tag{3a}$$

where $\alpha(\theta)$ is given by Eq. 1a, and the factor K, which corrects the measured irradiance for the non-linear imaging, is

$$K = M^2\frac{\alpha}{\theta}\frac{d\alpha}{d\theta} \tag{3b}$$

From Eq. 1a it can be derived that for $\theta = \alpha = 0$ the correction factor becomes $K_0 = [M(1-\varepsilon)/(1+\varepsilon)]^2$. Fig. 3(e) presents the relative correction factor

$$K^* = K/K_0 \tag{3c}$$

Finally, the radiance $L_r(\theta_r, \varphi_r) = I_r(\theta_r, \varphi_r)/A$, where A is the scattering (and illuminated) area of the sample. Hence, with $E_{cor}\theta_r d\theta_r d\varphi_r = I_r \sin\theta_r d\theta_r d\varphi_r$, it follows that the radiance can be obtained from the polar diagram of the corrected irradiance $E_{cor}(\theta_r, \varphi_r)$ via $L_r(\theta_r, \varphi_r) = E_{cor}(\theta_r, \varphi_r)\theta_r/(A\sin\theta_r) = E_{cor}(\theta_r, \varphi_r)/(A\,\mathrm{sinc}\,\theta_r)$.

2.5. Reflectance spectra

The reflectance spectrum of an object can be measured by taking images with the scatterometer for a series of quasi-monochromatic illuminations, using either a monochromator or interference filters. The latter method is used to determine the reflectance spectrum of scales of *Callophrys rubi*.

3. Results

3.1. Calibrations

The first step in validating the scatterometer, its calibration, was performed with the primary light beam, reflected by a small mirror positioned in the plane of F_1 (Fig. 1). The angular aperture of the primary light beam was 8.5^o. The mirror was rotated around a horizontal axis in steps of 5°, resulting in steps of the angle of the reflected beam, θ, of 10°. The reflected light distribution was recorded, and the resulting images were superimposed (Fig. 3(a)). The pixel position at the center of each of the spots was determined, and subsequently their distance, p, to the axial pixel (the pixel corresponding to the system axis: $p = 0$) was calculated. The distances p were then normalized, yielding the relative pixel distances: $p^* = p/p_{max}$.

These relative pixel distances are plotted in Fig. 3(c) as a function of the angle of the reflected beam, θ. The continuous curve in Fig. 3(c) is the theoretical curve $p^* = \alpha/\alpha_{max}$ obtained with Eq. 1a,b and $\varepsilon = 0.82$. The images of Fig. 3(a), obtained with the Olympus camera, yielded $p_{max} = 1145$, so that $M = p_{max}/\alpha_{max} = 5800$ pixels rad^{-1} = 101 pixels degree^{-1}.

The next calibration step concerned the secondary beam. The small mirror in the plane of F_1 was therefore put in a stable, approximately vertical position, and the vertical position of diaphragm D_4 was varied in steps of 0.5 mm. Figure 3(b) shows a superposition of every third of the obtained images. The pixel values of the spot centers were determined, and then their distance to the axial pixel ($p = 0$) was normalized to p_{max}. The position of the diaphragm with respect to the axial position, d, reaches an extreme value, d_{max}, when the angle of incidence $\theta_i = \theta_{max} = 90^o$. The pixel distance of the spot center then is p_{max}.

The plane of diaphragm D_4 is via the beam splitter conjugated to plane I, which is imaged at camera C_2. Formally, when the angle of the light beam with the secondary axis leaving lens L_5 equals α, then $d = \alpha f_5$ (f_5 is the focal length of lens L_5), so that $p^* = p/p_{max} = \alpha/\alpha_{max} = d/d_{max} = d^*$, where d^* is the relative diaphragm displacement. Indeed, as shown by Fig. 3(d), the pixels receiving the reflections from the successive illuminations are linearly related to the displacement of the diaphragm. The angle of incidence of the secondary beam, θ, thus can be immediately obtained from the diaphragm displacement, d, via the inverse expression of Eq. 1a:

$$\theta = \mathrm{asin}[\,(1-\varepsilon^2)\sin\alpha/(1+\varepsilon^2 - 2\varepsilon\cos\alpha)] \tag{4a}$$

and

$$\alpha = (\alpha_{max}/d_{max})\,d = \alpha_{max}d^* \tag{4b}$$

Figure 3(f) presents θ as a function of the relative diaphragm displacement $d^* = d/d_{max}$. In our setup $d_{max} = 11.0$ mm, in accordance with $d_{max} = f_5 \cdot \tan(\alpha_{max})$, where $f_5 = 55$ mm is the focal length of lens L_5.

(a)   (b)

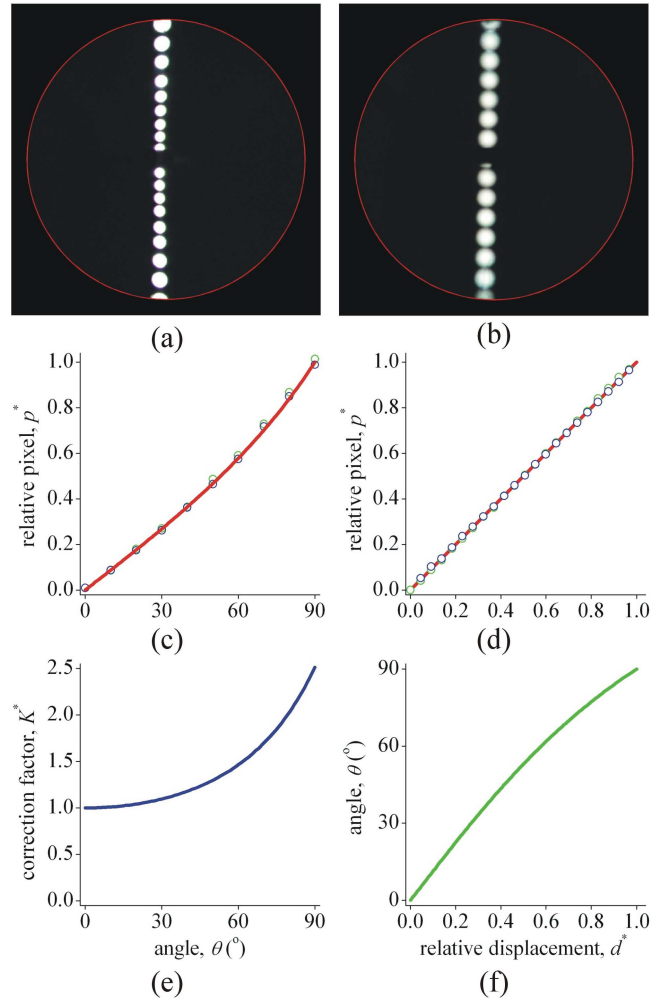(c)   (d)

(e)   (f)

Fig. 3. Calibration of the scatterometer with a small mirror, positioned in focal point F_1 of the scatterometer. (a) The mirror, reflecting the primary light beam, was rotated around a horizontal axis in steps of 5°, and the images of the light beam were superimposed. A light spot is missing in the center, because the mirror blocks the reflection of the axial beam. (b) The mirror, reflecting the secondary light beam, was in an approximately vertical position, and the vertical position of diaphragm D_4 (Fig. 1) was varied in steps; the resulting images were superimposed. The step size of the diaphragm was 0.5 mm, but only every third image was used in the superposition. (c) The centers of the image spots of (a) were determined, and their distance to the axial pixel was then normalized to the value obtained with a mirror angle of 45°, which corresponds to an angle of the reflected beam $\theta_{max} = 90^\circ$. (d) The centers of the image spots of (b) were determined, and the distances to the axial pixel, normalized to the maximal value, were plotted as a function of the relative displacement d^* of diaphragm D_4 in the secondary beam. (e) Relative correction factor K^* for the radiance in a polar plot (Eq. 3c). (f) Relationship between the angle of illumination, θ, and relative diaphragm position, d^* (Eq. 4). The red circles in (a) and (b) indicate the boundary of the image corresponding to $\theta_{max} = 90^\circ$. The blue and green symbols in (c) and (d) represent the image spots above ($\varphi_r = \pi/2$) and below ($\varphi_r = 3\pi/2$) the horizontal axis, respectively. The image spots are not perfectly in a vertical plane, because the mirror plane and the rotation axis of the pin, to which the mirror is glued, were not perfectly parallel.
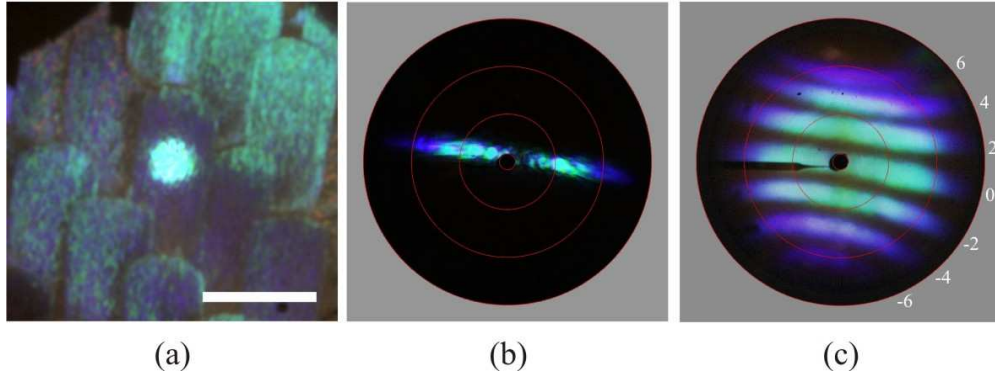
Fig. 4. Scattering by a dorsal wing scale of the butterfly *Morpho aega*. (a) A small wing fragment was positioned in the scatterometer and the primary beam was projected as a 40 μm spot at a single scale (a much wider area was illuminated by a weaker beam delivered by the secondary source); bar 100 μm. (b) The scattering pattern resulting from the primary beam. (c) Scattering patterns created by the secondary beam with diaphragm D_4 positioned at $d = 0, \pm2, \pm4$, and ±6 mm with respect to the axis (corresponding to an angle of incidence of $\theta_i = 0^o$, $\pm20.5^o, \pm39.9^o$ and $\pm57.1^o$, respectively). The long, pointed, black object at 9 o'clock is the glass micropipette holding the about circular wing fragment. The red circles in (b) and (c) indicate scattering angles of $\theta_r = 5, 30, 60$, and 90 degrees.

3.2. Scattering by wing scales of the butterfly Morpho aega

The power of the imaging scatterometer was investigated on a small fragment of the dorsal wings of *Morpho aega*, a highly iridescent butterfly. The primary beam with aperture 8.5^o was focused on one of the scales, resulting in a 40 μm diameter spot (Fig. 4(a)). The light scattered by the scale had a spatial distribution almost restricted to a plane oriented perpendicular to the longitudinal ridges of the scale (Fig. 4(b)). The lateral spread of the light scattering in that plane is wider for light of short wavelengths than for light of long wavelengths. The scattering pattern is somewhat patchy, which is due to the not fully regular organization of the ridges. Minor movements of the scale, so that the focusing spot occurred at slightly different locations, resulted in abrupt changes of the patches.

Widening the area of illumination resulted in a smoother pattern as is illustrated in Fig. 4(c), where the secondary beam was applied. Here the illumination spot was about 130 μm; the diameter of diaphragm D_4 was 1.5 mm, meaning an aperture of about 16°, decreasing however with increasing angle of incidence (see Fig. 3(c)). Figure 4(c) presents superimposed scattering diagrams resulting from illuminations with the secondary beam diaphragm D_4 at positions d = -6, -4, -2, 0, 2, 4, and 6 mm, respectively. With d_{max} = 11 mm, it follows from Fig. 3(f) (or Eq. 2) that d = 2, 4, 6 mm corresponds to an angle of incidence of θ = 20.5^o, 39.9^o, and 57.1^o, respectively.

3.3. Reflectance of Callophrys rubi scales

The imaging scatterometer allows straightforward measurement of reflectance spectra. As an example, Fig. 5 shows measurements of a scale on the ventral wing of the lycaenid butterfly *Callophrys rubi*. The scale was illuminated by the primary, narrow beam focused at a 40 μm diameter spot (Fig. 5(a)). The scale appeared to consist of yellow and bluish reflecting microdomains [4,19]. The incident light was scattered into a very wide angle (Fig. 5(b)). Applying monochromatic light and using the reflection from a mirror as reference, the reflectance was calculated by integrating the reflection from spatial areas bounded by cones with apertures 30°, 60°, and 90° (Fig. 5(c)). The resulting spectra are approximately proportional to each other, and thus the scale, although structurally colored, scatters light into a wide angle. (The contributions to the reflectance by the wing substrate and other scales on the wing are minor, as will be described elsewhere.)
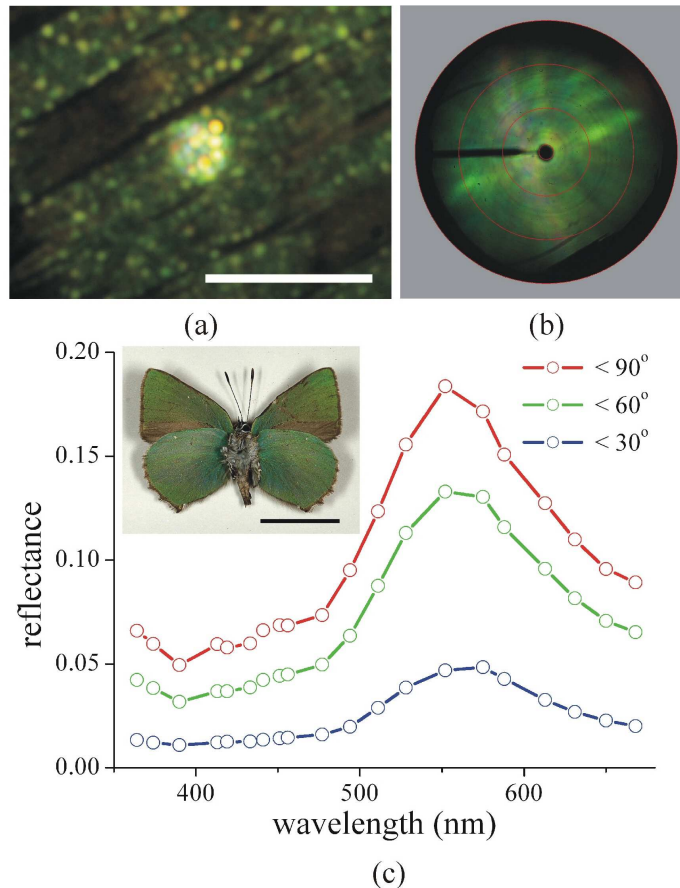
(a)

(b)

(c)

Fig. 5. Scattering characteristics of the ventral wings of the Green Hairstreak, *Callophrys rubi*. (a) A small wing fragment was positioned in the scatterometer, and the primary beam was projected as a 40 μm spot at a scale (a wider secondary light beam caused the additional scattering of the scale assembly); bar 100 μm. (b) The scattering pattern is quite random and covers a major part of the hemisphere. (c) The integral of the scattered light for circular areas bounded by scattering angles $\theta_r = 30°$, $60°$, and $90°$ was divided by the incident light flux, resulting in reflectance spectra that peak in the green wavelength range (inset: the ventral side of the Green Hairstreak; bar 1 cm).

4. Discussion

The imaging scatterometer described here consists of standard optical elements, except for the ellipsoidal mirror, which had to be custom built. The heart of the design is the property of an ellipsoidal mirror that it compresses a hemispherical space into a small cone, which then allows projection by common lenses. The system has an essential, sensitive point in that the scattering sample has to be positioned quite accurately in the ellipsoid's first focal point. In practice this is achieved by observing the sample with the binocular viewer to which camera C_1 is connected, and furthermore by checking that all reflected light rays are passing a narrow diaphragm surrounding the second focal point, F_2 (Fig. 1). The unique power of the instrument is that it visualizes the near-field properties of the sample (with camera C_1), and simultaneously visualizes the far-field, hemispherical scattering properties of the study object (with camera C_2).

After completion of our instrument we found, not fully to our surprise, that scatterometers with related designs were reported before. The most similar arrangement is that developed for

studying aerosols by Chang and co-workers [20,21]. Their ellipsoidal mirror also has a central hole through which the (only) illuminating beam is applied. A single lens images the scattered light directly at a digital camera, and thus a spatial filter for blocking transmitted light cannot be employed. A slightly different scatterometer, also employing an ellipsoidal reflector, was developed by Rodríguez-Herrera et al. [22] for studying the scattering by rough surfaces. Their laser beam is reflected by a 45° beam splitter, similar to the secondary beam of Fig. 1. The scatterometer described in the present paper appears to combine a number of solutions of the other systems. It has substantial versatility for studying the optics of small scale objects.

Previous studies of the scattering by *Morpho* wing scales, illuminated more or less perpendicularly, have demonstrated a highly directional reflection in the plane of the scale ridges and a broad diffraction in the perpendicular plane. The more or less line-shaped far-field scattering pattern [14,15,17,23] has been interpreted with an optical model that treats the ridges as a pile of equidistant, reflecting plates [15]. When the direction of the incident light beam deviates from the normal, the shape of the scattering pattern becomes slightly curved (Fig. 4(c); see also Fig. 8.22 of [24], and [25]). A quantitative interpretation of this phenomenon will be presented elsewhere (in preparation).

The scattering of the dorsal wing scales of many lycaenids is highly directional, resulting in a spatially limited scattering diagram [26]. However, the scattering pattern of the ventral wing scales of the lycaenid *Callophrys rubi* covers almost the full hemisphere, causing the matte appearance of the lycaenid in the resting state, when the wings are closed. The green peaking reflectance spectrum (Fig. 5(c)), calculated by integration of the scattering pattern, nicely matches the reflectance spectrum of leaves, thus ensuring excellent camouflage in the natural habitat [4,19].

The reflectance spectrum can be alternatively -and more easily- obtained by using an integrating sphere, but the advantage of the scatterometer is that it allows the much more detailed measurement of the directional reflectance, or, the detailed bidirectional reflectance distribution function. The scatterometer measurements will be helpful to understand the light scattering characteristics of butterfly scales, and hence provide insight into butterfly coloration and its biological function. Of course, the scatterometer can also be used to visualize the scattering patterns of small objects other than butterfly scales. We have successfully explored bird feathers, beetle cuticle, and similar biological tissues with structural coloration.

Acknowledgments